Icarus 202 (2009) 414–428

Contents lists available at ScienceDirect

Icarus

www.elsevier.com/locate/icarus

Effects of surface roughness and graybody emissivity on martian thermal infrared spectra

Joshua L. Bandfield *

Department of Earth and Space Sciences, University of Washington, Seattle, WA 98195-1310, USA

ARTICLE INFO

Article history:
Received 29 December 2008
Revised 20 March 2009
Accepted 23 March 2009
Available online 1 April 2009

Keywords:
Mars, surface
Spectroscopy
Radiative transfer

ABSTRACT

Slopes are present in martian apparent surface emissivity observations collected by the Thermal Emission Spectrometer (TES) and the Thermal Emission Imaging System (THEMIS). These slopes are attributed to misrepresenting the surface temperature, either through incorrect assumptions about the maximum emissivity of surface materials or the presumption of a uniform surface temperature within the field of view. These incorrect assumptions leave distinct characteristics in the resulting apparent emissivity data that can be used to gain a better understanding of the surface properties. Surfaces with steep slopes typically have a variable surface temperatures within the field of view that cause distinct and highly variable slopes in apparent emissivity spectra based on the observing conditions. These properties are documented on the southwestern flank of Apollinaris Patera and can be reasonably approximated by modeled data. This spectral behavior is associated with extremely rough martian surfaces and includes surfaces south of Arsia Mons and near Warrego Valles that also appear to have high slopes in high resolution images. Surfaces with low maximum values of emissivity have apparent emissivity spectra with more consistent spectral slopes that do not vary greatly based on observing conditions. This spectral surface type is documented in Terra Serenum and is consistent with associated high resolution images that do not indicate the presence of a surface significantly rougher that the surrounding terrain.

1. Introduction

Thermal infrared (TIR) measurements are sensitive to a large variety of surface and atmospheric properties. For example, TIR measurements of the martian surface from orbit are directly affected by the surface temperature and composition and the atmospheric temperature structure, pressure, and composition. Accurate determination of these properties can be used to determine a wide variety of present and past processes, such as the aqueous and igneous history of the crust inferred from surface mineralogy or the present distribution and dynamics of water in the subsurface, surface, and atmosphere.

This variety of sensitivities leads to complex datasets that require a thorough understanding of the interaction of surface and atmospheric compositional and thermophysical properties in order for their effects to be accurately separated and interpreted. In addition, the effect of assumptions in data processing and interpretation that are generally considered safe under most circumstances should be periodically re-evaluated to ensure that critical factors have not changed.

Evaluation of the TIR spectral properties of surfaces requires the removal of temperature effects from the measurements in order to isolate the typically temperature independent spectral properties (e.g. Gillespie et al., 1998). This requires knowledge of the distribution of surface kinetic temperatures within the measurement field of view (FOV). It has generally been assumed with martian TIR datasets that the surface within the FOV is of a uniform temperature and that the maximum emissivity is unity at some point within the wavelength coverage of the measurement (e.g. Christensen et al., 2001). In addition, it is sometimes assumed that the atmosphere is transparent at the wavelength of assumed unit emissivity.

The effects of assuming a FOV of uniform temperature on TIR data has been investigated in a variety of terrestrial studies (e.g. Balick and Hutchinson, 1986; Smith et al., 1997; Zhang et al., 2004; McCabe et al., 2008). These studies have typically focused on the effects of vegetation and directionality on surface temperatures derived from broadband measurements (e.g. Li et al., 2004). The anisothermality investigations were not typically linked to surface roughness because the sub-pixel variation in temperature is primarily due to vegetation rather than slopes on bare surfaces. Other applications include the detection of volcanic activity where extreme temperature contrasts are present between lava flows and the surrounding terrain within the FOV (Ramsey and Kuhn, 2004).

* Fax: +1 206 543 0489.
E-mail address: joshband@u.washington.edu.

0019-1035/$ – see front matter
doi:10.1016/j.icarus.2009.03.031

The assumptions of a uniform surface temperature and a maximum emissivity of unity are commonly met closely enough that they have little effect on subsequent mineralogical interpretations, especially under laboratory conditions (Ruff et al., 1997). Where significant deviations from unit maximum emissivity or uniform surface temperature occur, the resulting apparent emissivity spectra have significant spectral slopes present (e.g. Ruff et al., 1997; Gillespie et al., 1998). This effect occurs because of the highly non-linear nature of Planck radiance as a function of temperature and wavelength. An anisothermal surface consists of a mixture of Planck radiance from a variety of temperatures. This radiance cannot be reproduced by Planck radiance of a single temperature. The effect is similar for a surface that has a uniform, but non-unit, (graybody) emissivity when the maximum emissivity is assumed to be unity. In addition to affecting the apparent emissivity of the measured surface, anisothermality and graybody emissivity can result in errors in the derived surface kinetic temperature (e.g. Gillespie et al., 1998; McCabe et al., 2008). These errors can commonly exceed several degrees, which is larger than is necessary to accurately monitor planetary surfaces and serve as proper inputs for climate and thermophysical models.

Although spectral slopes may present an additional difficulty in the interpretation of the data, they can also be used to better understand the physical and compositional properties of a surface. For example, Christensen (1986) and Nowicki and Christensen (2007) used anisothermal effects present in Viking Infrared Thermal Mapper and Mars Global Surveyor Thermal Emission Spectrometer (TES) nighttime data to predict the concentration of rocks on the martian surface based on their warm temperatures relative to cold finer materials. These effects have also been explored in detail for planetary surfaces by Colwell and Jakosky (2002) using lunar TIR observations to simulate the potential spectral effects of anisothermality. They noted that the apparent emissivity of surface observations can be significantly affected by surface slopes at low solar elevation angles and the effects can be minimized with observations collected at low phase angles.

Where TIR measurements have been used to derive surface roughness, the method is typically based on the reduction of spectral contrast due to reflections of emitted radiance between surfaces (e.g. Ramsey and Fink, 1999; Danilina et al., 2006; Mushkin et al., 2007). This effect is distinct from that of anisothermality on TIR spectra and generally is sensitive to scales of less than a few millimeters that are not thermally isolated.

The work presented here is motivated by martian TIR observations that have shown effects of anisothermality and non-unit emissivity. Bandfield and Edwards (2008) used multi-directional TIR observations from the TES to document the effects of anisothermality within the measurement FOV. By observing a surface from a variety of angles, the relative proportions of warm sunlit versus cool shaded surfaces varies predictably. The magnitude of the apparent change in temperature with the changing observation geometry was used to derive surface slope characteristics. Bandfield and Edwards (2008) used only bolometric broadband measurements, but similar tools developed for that work can be applied to derivation of surface roughness by applying the same principles to nadir spectral measurements. In this case, strong anisothermality within the FOV will not be well approximated by a Planck function from a single temperature and the resulting apparent emissivity spectrum will have a significant slope.

Osterloo et al. (2008) have documented spectral slopes present in both TES and 2001 Mars Odyssey Thermal Emission Imaging System (THEMIS) data. In this case, the spectral slopes were interpreted to be the result of relatively low emissivity across the wavelength range of the measurement. Although a unique spectral match could not be made, Osterloo et al. (2008) note that this property is unusual among geologic materials, one exception being chlorides. This conclusion is supported by the morphological characteristics of the spectrally unique surfaces.

Why is a spectral slope interpreted as non-unit emissivity in one case and as anisothermality in the other? Under certain circumstances, it is difficult to distinguish between these two properties. However, with repeat coverage at a variety of local times and seasons and with more extensive wavelength coverage, the surface anisothermality and non-unit emissivity have different behaviors that can be leveraged in a way to uniquely identify their effects. The purpose of this work is to demonstrate that these effects are present in both TES and THEMIS data and to separate their causes based on radiative and thermophysical models. By applying quantitative methods to the measurements, the interpretations based on the data are more robust and it is possible to extract quantitative information, such as surface slope distributions.

2. Methods

2.1. Description of TES and THEMIS instruments and data

The thermal infrared imager on THEMIS consists of a 320 by 240 element uncooled microbolometer array with 9 spectral channels centered at wavelengths between ~7 and 15 μm and a spatial sampling of 100 m. More detailed descriptions of calibration methods and radiometric uncertainties are presented in Christensen et al. (2004) and Bandfield et al. (2004). The TES instrument is a Fourier transform Michelson interferometer that covers the wavelength range from 1700 to 200 cm^{-1} (~6 to 50 μm) at 10 or 5 cm^{-1} sampling. Three cross-track and two along-track detectors provide a spatial sampling of 3 by ~8 km. A more complete description of the TES instrument, operations, and radiometric calibration can be found in Christensen et al. (2001).

All data used in the analyses presented here were acquired at afternoon local times of ~1400–1800 h and at nadir observation geometries with emission angles of close to 0°. THEMIS "4-panel" images were used to identify regions with spectral slopes. These images have been used to rapidly identify spectrally unique surfaces using a variety of the THEMIS spectral radiance channels displayed in 3 separate decorrelation stretch (DCS; Gillespie et al., 1986) images along with the corresponding temperature image (e.g. Bandfield, 2006, 2008). Surface emissivity spectra were obtained using atmospheric correction methods described in Bandfield et al. (2004) for THEMIS data and Bandfield (2008) for TES data.

Briefly, THEMIS data are corrected by assuming a uniform atmosphere over the scene of interest. Atmospheric emission and scattering are characterized and removed using a surface of assumed uniform composition, but variable temperature. Lower spatial resolution TES data are used to determine surface emissivity (e.g. Smith et al., 2000a; Bandfield and Smith, 2003; Bandfield, 2008) over a relatively uniform region to characterize atmospheric attenuation. The atmospheric properties can be subtracted and divided out of the THEMIS data on a per pixel basis allowing for the recovery of full resolution surface emissivity.

TES data are corrected using a nearby high albedo, dusty surface, which has been well characterized spectrally (Bandfield and Smith, 2003). Minor gas absorptions are removed using the method of Bandfield and Smith (2003) and opacity is determined using the high albedo surface of known emissivity, atmospheric temperature profile (Conrath et al., 2000), and the simplified plane-parallel, non-scattering radiative model of Smith et al. (2000b). Atmospheric opacity is scaled to the surface pressure at the local region of interest and with the local temperature profile, the surface emissivity at the area of interest is directly calculated. The advantage of this technique, despite requiring relatively ice-free conditions and a local dusty surface, is that it does not require

special multiple emission angle observations or a predetermined set of surface compositions.

Some of the assumptions in the processing of the data are invalid because of the anisothermal or non-unit emissivity nature of the surfaces investigated here. This primarily occurs where measured radiance is divided by Planck radiance at the wavelength of the highest brightness temperature. However, the simulation and modeling of the data described below explicitly incorporate the same assumptions and allow for direct comparison and determination of surface properties.

In addition to the TIR datasets, high-resolution images (<6 m/pixel sampling) from the Mars Global Surveyor Mars Orbiter Camera (MOC, Malin and Edgett, 2001) and the Mars Reconnaissance Orbiter High Resolution Imaging Science Experiment (HiRISE, McEwen et al., 2007) and Context Imager (CTX, Malin et al., 2007) was used to identify rough surface textures that would cause a high degree of anisothermality that could result in TIR spectral slopes.

2.2. Surface roughness model

In order to predict the effects of anisothermality on the measured spectra, it is necessary to use a realistic distribution of temperatures for a surface associated with a particular observation. This requires both a model for the realistic distribution of surface slopes and the ability to predict the temperature of each of those slopes. The approach of Bandfield and Edwards (2008) is taken here, which uses the θ-bar parameter described by Hapke (1984) to describe the distribution of surface slopes using only one free parameter. This is a model based on a Gaussian distribution of slopes along a cross section of a surface assuming a random distribution of slope azimuths. Although surface slope distributions may be more complicated, there is not enough leverage in the data to allow for the use of more detailed surface slope distribution models. The use of the θ-bar parameter allows for a simple quantitative derivation of surface roughness that permits direct comparisons of surfaces across the planet (Bandfield and Edwards, 2008). Higher values of θ-bar have greater proportions of steeper slopes in the slope distribution model.

A thermal model is applied to each slope/azimuth orientation to predict the range of surface temperatures. The KRC thermal model (H.H. Kieffer, manuscript in preparation) is used here as it has been used successfully for modeling variety of complex surface types, including layered surfaces, ices, and surface slopes using both orbital and in situ datasets (e.g. Titus et al., 2003; Armstrong et al., 2005; Kieffer et al., 2006; Fergason et al., 2006a, 2006b; Bandfield and Edwards, 2008; Bandfield and Feldman, 2008). When applied to daytime data, the model has large uncertainties due to uncertainties in direct and scattered solar radiance and surface albedo. However, differences in surface temperatures between sunlit and shaded slopes are the driving factor in producing spectral slopes. As a result, these uncertainties cancel out to a large degree. Bandfield and Edwards (2008) investigate these uncertainties in detail.

The nadir orientation of the measurements used for this study prevents the necessity of accounting for obscuration of surfaces behind others in the FOV. Hard shadows cast onto other surfaces are not accounted for in the model, however. This is generally not an important factor for most surfaces, but may play an increasing role for extremely rough surfaces when the Sun is close to the horizon. Properly accounting for these surfaces requires much more sophisticated modeling that is beyond the scope of the work presented here.

The modeled surface temperature Planck radiance for each surface slope and azimuth combination is calculated. The simulated radiance within the FOV is calculated by summing the radiance of each slope and azimuth combination weighted by the areal coverage that is predicted by the θ-bar surface slope distribution model. For this work, several values of θ-bar are used to produce several sets of simulated data, which are then compared to the TES and THEMIS measurements.

The radiance is calculated at the TES 10 cm^{-1} sampling. To produce simulated radiance as measured by THEMIS, the mixture of Planck radiances is convolved using the THEMIS spectral bandpass filter functions. The simulated radiance is then converted to emissivity by dividing out the Planck radiance for the brightness temperature determined at 1308 cm^{-1} for the simulated TES data or THEMIS band 3. This is the same method applied to the TES and THEMIS measurements and allows for a direct comparison of the measured and modeled apparent emissivities. Actual (rather than apparent) surface emissivity is assumed to be that of surface dust (Bandfield and Smith, 2003), which is relatively featureless and only contributes a small spectral slope between ~800–1200 cm^{-1}. The dust spectral shape is an average of many observations and the simulated TES spectra have significantly lower noise than the TES observations of the surfaces of interest.

2.3. Atmospheric effects on low emissivity (high reflectivity) surfaces

Understanding the spectral behavior of non-unit emissivity surfaces in natural environments can be complex because of the interfering effects of the atmosphere and the inability to accurately estimate the surface kinetic temperature remotely. Unfortunately, it is impossible to truly separate emissivity and temperature effects from the remote sensing measurements because there is no safe assumption that can be made about either the temperature or the emissivity of the surface. This problem can be summarized by the following set of equations describing a series of observations:

$$\begin{aligned}
\underline{R_{\mathrm{meas1}}} &= B_{\mathrm{surf1}} \cdot \varepsilon_{\mathrm{surf}} \cdot \underline{e^{-\tau_{\mathrm{atm}}}} + \underline{R_{\mathrm{atm}}} \cdot (\underline{1} - \varepsilon_{\mathrm{surf}}) + \underline{R_{\mathrm{atm}}},\\
\underline{R_{\mathrm{meas2}}} &= B_{\mathrm{surf2}} \cdot \varepsilon_{\mathrm{surf}} \cdot \underline{e^{-\tau_{\mathrm{atm}}}} + \underline{R_{\mathrm{atm}}} \cdot (\underline{1} - \varepsilon_{\mathrm{surf}}) + \underline{R_{\mathrm{atm}}},\\
\underline{R_{\mathrm{meas3}}} &= B_{\mathrm{surf3}} \cdot \varepsilon_{\mathrm{surf}} \cdot \underline{e^{-\tau_{\mathrm{atm}}}} + \underline{R_{\mathrm{atm}}} \cdot (\underline{1} - \varepsilon_{\mathrm{surf}}) + \underline{R_{\mathrm{atm}}}, \ldots . \qquad (1)
\end{aligned}$$

R_{meas} is the measured radiance, B_{surf} is the Planck radiance for the kinetic temperature of the measured surface, $\varepsilon_{\mathrm{surf}}$ is the surface emissivity, τ_{atm} is the atmospheric opacity (which also has an unstated influence on R_{atm}), and R_{atm} is the upwelling and downwelling atmospheric radiance. All factors are wavelength dependent and known factors (or determined via other measurements) are underlined. With multiple measurements of a surface with (assumed) similar emissivity ($R_{\mathrm{meas1-3}}$) at different angles or temperatures, previous studies have gained some leverage on isolating the surface emissivity (e.g. Bandfield and Smith, 2003; Bandfield et al., 2004). However, these studies have relied on the crucial assumption of (near-)unit emissivity near at least one measurement wavelength, which allows for the determination of BB_{surf} and making the set of equations over- rather than underdetermined.

It is possible, however to forward model the predicted behavior of low emissivity surfaces and process them using the same assumptions and techniques applied to the TES and THEMIS data. This allows for a direct comparison and the ability to predict the general behavior of these types of surfaces in the data.

The simulated surface radiance is calculated assuming a variety of graybody emissivity values. The generally low emissivity values result in a relatively high proportion of reflected atmospheric downwelling radiance that can have a significant influence on the resulting apparent emissivity. This is calculated assuming Kirchoff's Law (reflectivity = 1 − emissivity) and the same simplified atmospheric model mentioned above. The magnitude of the effect of downwelling radiance on the apparent emissivity is proportional

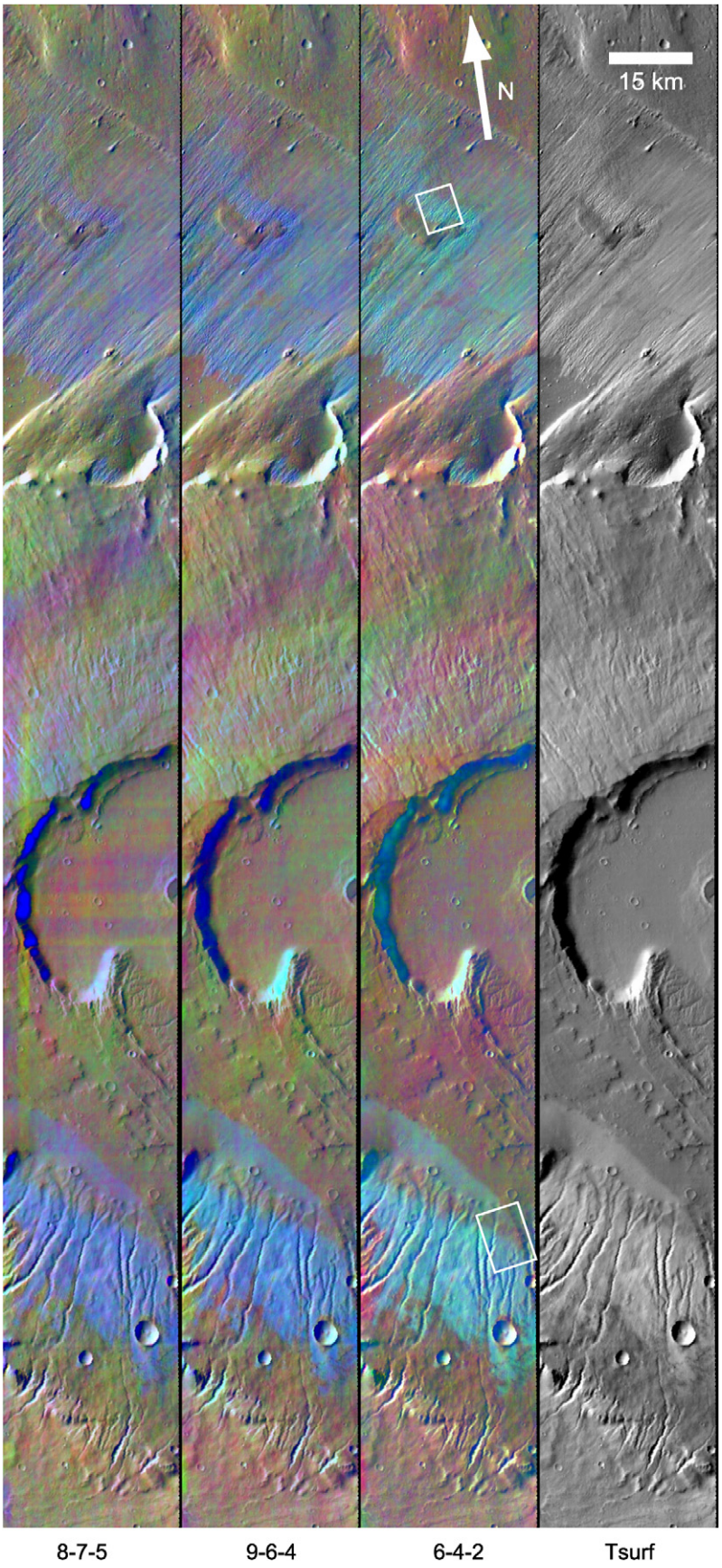

Fig. 1. THEMIS 4-panel image I02740006 covering a portion of Apollinaris Patera and centered near 174° E, 8° S. The three images on the left are decorrelation stretch images of THEMIS multispectral data using bands 8-7-5, 9-6-4, and 6-4-2. The fourth image is the derived surface temperature. The regions on the southern flank and immediately north of the volcano that appear variable shades of blue contain the spectral slopes that are discussed in the text. The white boxes indicate regions of visible images shown in Fig. 4. (For interpretation of the references to color in this figure legend, the reader is referred to the web version of this article.)

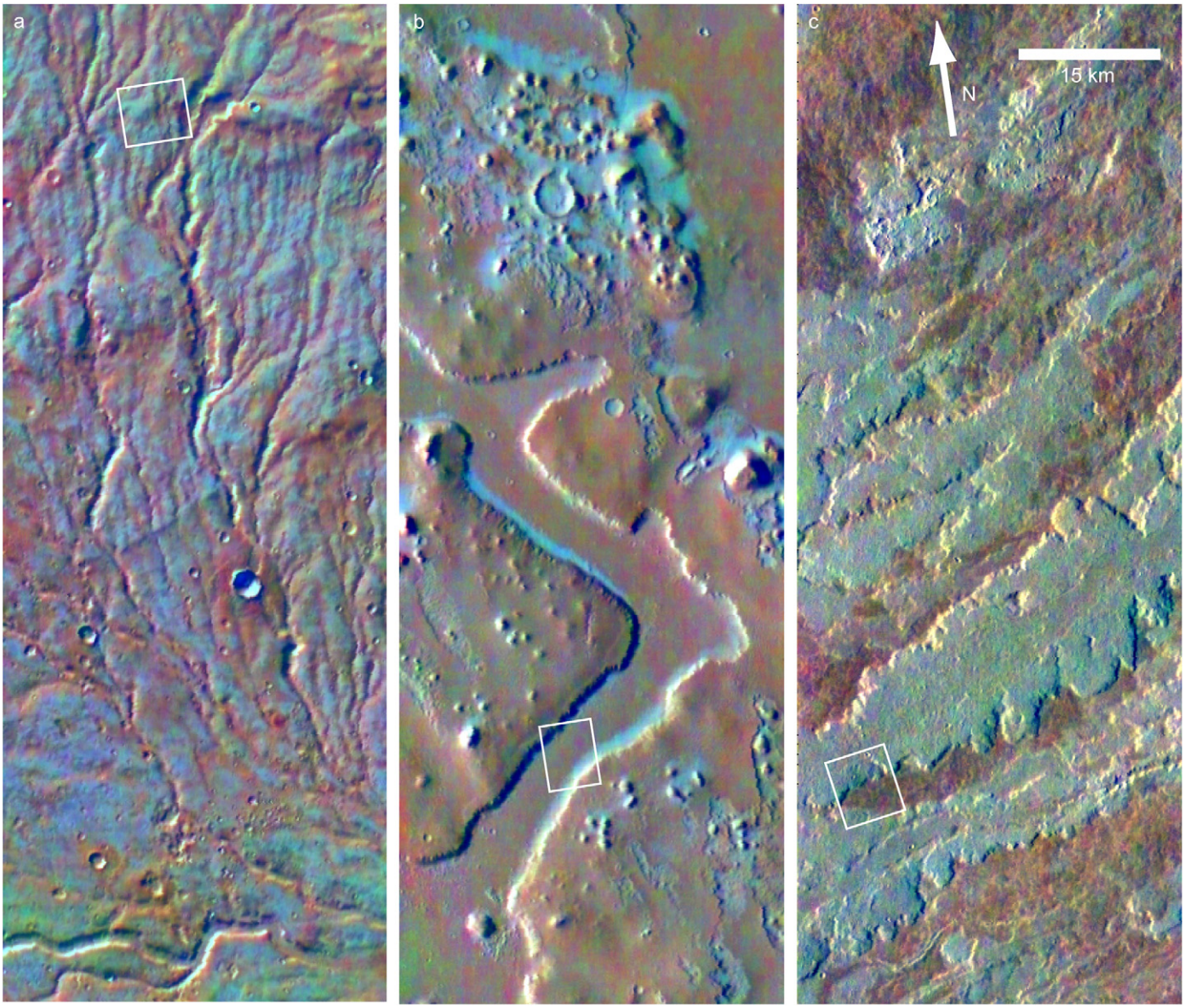

Fig. 2. Band 6-4-2 decorrelation stretch images of regions with similar spectral character as the example shown in Fig. 1. (a) Valley networks near Warrego Valles (I01714004) centered near 266.9° E, 41.5° S. (b) Lucus Planum (I02265009) centered near 193.85° E, 1.75° N. (c) Lava flows south of Arsia Mons (I17841001) centered near 233.25° E, 17.0° S. The white boxes indicate regions of visible images shown in Fig. 4.

to the surface reflectivity and the relative difference in the magnitudes of the surface radiance and downwelling radiance. These effects have been documented in detail by Ruff et al. (2006). TES temperature profiles and atmospheric dust opacities from the same location and season as the observation (Smith, 2004) are input into the simplified model in a manner similar to Smith et al. (2000a) and Bandfield and Smith (2003).

3. Observations

Examples of these effects in the TES and THEMIS measurements are described here in detail. These measurements are compared to simulated data assuming anisothermal or low emissivity conditions as described above. The extent of similar patterns in the data are also investigated to the extent that high quality THEMIS data coverage exists. The two similar but distinct surface spectral types generally contain significant negative slopes with increasing wavelength, but there are significant differences in their behavior as a function of temperature and solar inclination. To illustrate the spectral behavior, the spectral analysis focuses on two representative locations that have repeat TES and THEMIS coverage under a variety of conditions.

3.1. Apollinaris patera type example

Fig. 1 shows a 4-panel image that covers part of Apollinaris Patera, a volcano located near 174° E, 8.5° S. Each of the 3 DCS images have a unit that is varying shades of blue in color relative to the surrounding terrain. The DCS images provide relative spectral information and the blue color indicates that there is a consistent negative spectral slope with increasing wavelength present over the blue surfaces relative to the other surfaces. There are two distinct blue unit surfaces in Fig. 1 that are correlated with yardangs directly to the north of the volcano and more loosely correlated with erosional channels on the southwest flank of the volcano.

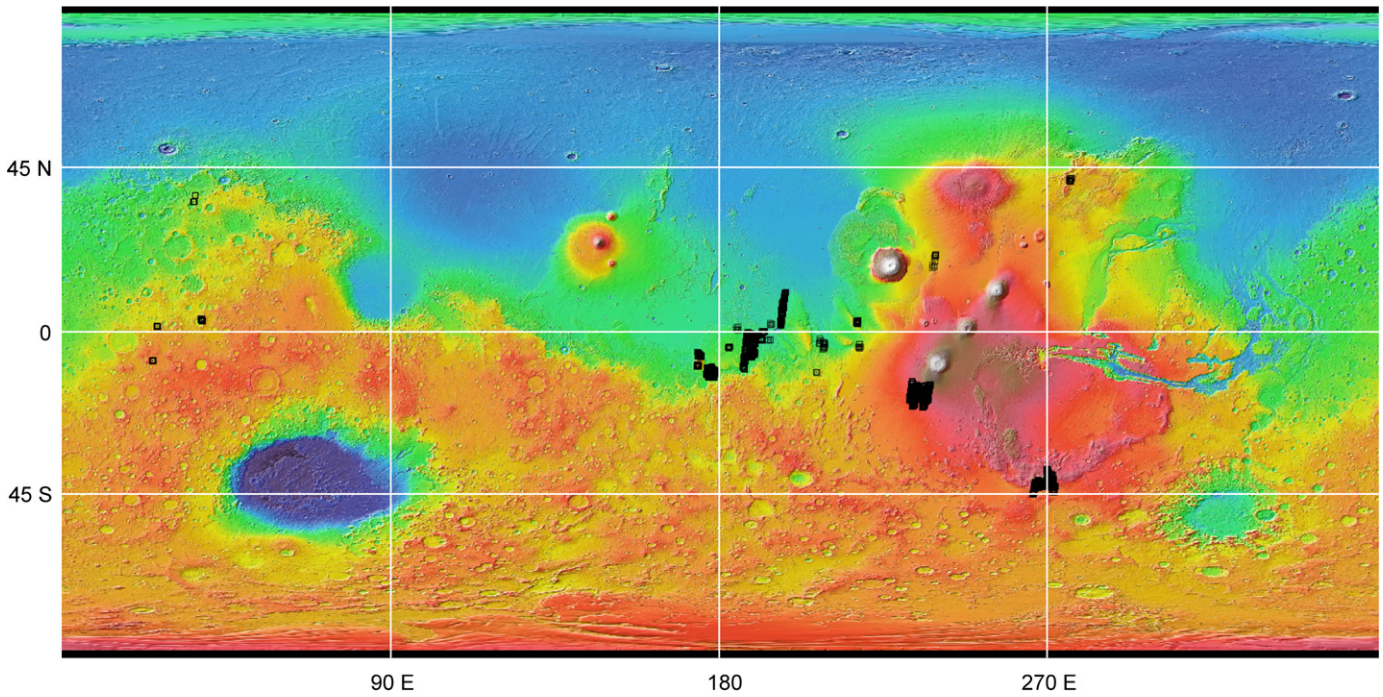

Fig. 3. The global distribution of surfaces that have color patterns similar to those shown in Figs. 1 and 2 and likely due to anisothermal surfaces with high slopes. Each box indicates the location of a contiguous unit within a THEMIS image. Because surface coverage is not complete, it is likely that this distribution is not complete. The background image is the global Mars Orbiter Laser Altimeter (MOLA) colorized shaded relief topographic map. (For interpretation of the references to color in this figure legend, the reader is referred to the web version of this article.)

Similar color patterns in the DCS images have been identified on several other regions (Fig. 2). These surfaces are concentrated between ∼170–270° E and −45–25° N, roughly coincident with the Tharsis region and to the west (Fig. 3). Several other exposures have been identified in other locations. The spectrally sloped surfaces were identified based on a qualitative assessment of THEMIS DCS images and subsequently confirmed via spectral analysis. The coverage of warm THEMIS images suitable for analysis is not complete (especially in the northern hemisphere) and errors of omission are also possible.

Where it was available, high-resolution images were examined over the surfaces of interest and several examples are shown in Fig. 4. In all instances, a high degree of surface roughness is present in the images. However, the specific morphology of the surfaces is variable. Surfaces near Warrego Vallis are composed of spherical/conical mounds several meters across. Surfaces north of Apollinaris Patera are composed of parallel and sharp linear ridges whereas ridges form a woven pattern within Lucus Planum (Fig. 4).

The southwest flank of Apollinaris Patera clearly displays the spectral slope effect in THEMIS data and there is repeat coverage by both TES and THEMIS at a variety of temperatures, and solar incidence angles (Table 1, Fig. 5). This coverage allows for excellent characterization of spectral properties that would clearly separate spectral slope effects due to anisothermality versus low emissivity. The spectral slopes are present in all of the 4 THEMIS images that cover the location but the magnitude of the slope varies by a factor of ∼5. No significant spectral slope is detected in the co-located TES data.

3.2. Terra Serenum type example

The second sloped spectral type has a distinct color combination in the THEMIS 4-panel DCS images (Fig. 6). The color is typically blue/turquoise/yellow-orange in the three DCS images, which generally indicates a negative spectral slope in the longer wavelength band combinations (bands 8/7/5 and 9/6/4 projected as red, green, and blue respectively). The last band combination (bands 6/4/2) is clearly distinct from the other sloped spectral type and its yellow-orange color indicates low emissivity at THEMIS band 2 relative to the surrounding terrain. It should be stressed that the colors present in DCS images are dependent on the relative differences between spectra present in the image. The spectral characteristics of the surrounding terrain typically present for the two surfaces is significantly different (dust with low emissivity in THEMIS band 2 in the former and basalt with high emissivity in the current example) and this difference may contribute to the different color combinations of the two spectral types in the THEMIS DCS images.

This is the same spectral unit that is described by Osterloo et al. (2008) and its general spectral character and distribution has been characterized along with the associated morphological properties. Occurrences are typically isolated local topographic depressions of $< \sim 100$ km^2 within low albedo regions of the southern highlands. The spectrally distinct unit appears lighter in tone relative to the surrounding terrain, though it is only typically ∼0.01 higher in albedo (Osterloo et al., 2008). Although the morphology does not appear smooth in high resolution images, hard shadows indicating steep slopes are not common as they are in the other surface typified by the southwest flank of Apollinaris Patera (Fig. 7).

A typical surface exposure of the sloped spectral unit with repeat TES and THEMIS coverage is located within an unnamed crater near 180.75° E, 27.25° S. As with the Apollinaris Patera example, measurements were acquired at a variety of temperatures and solar incidence angles, allowing for characterization of spectral properties that would clearly separate spectral slope effects due to anisothermality versus low emissivity. Spectral slopes appear similar in nature to the Apollinaris Patera example (Fig. 8). A distinct difference between the Apollinaris Patera and Terra Serenum data is present at the shortest wavelengths consistent with the differences observed in the DCS images. The Terra Serenum spectra also do not exhibit the significant variability between ob-

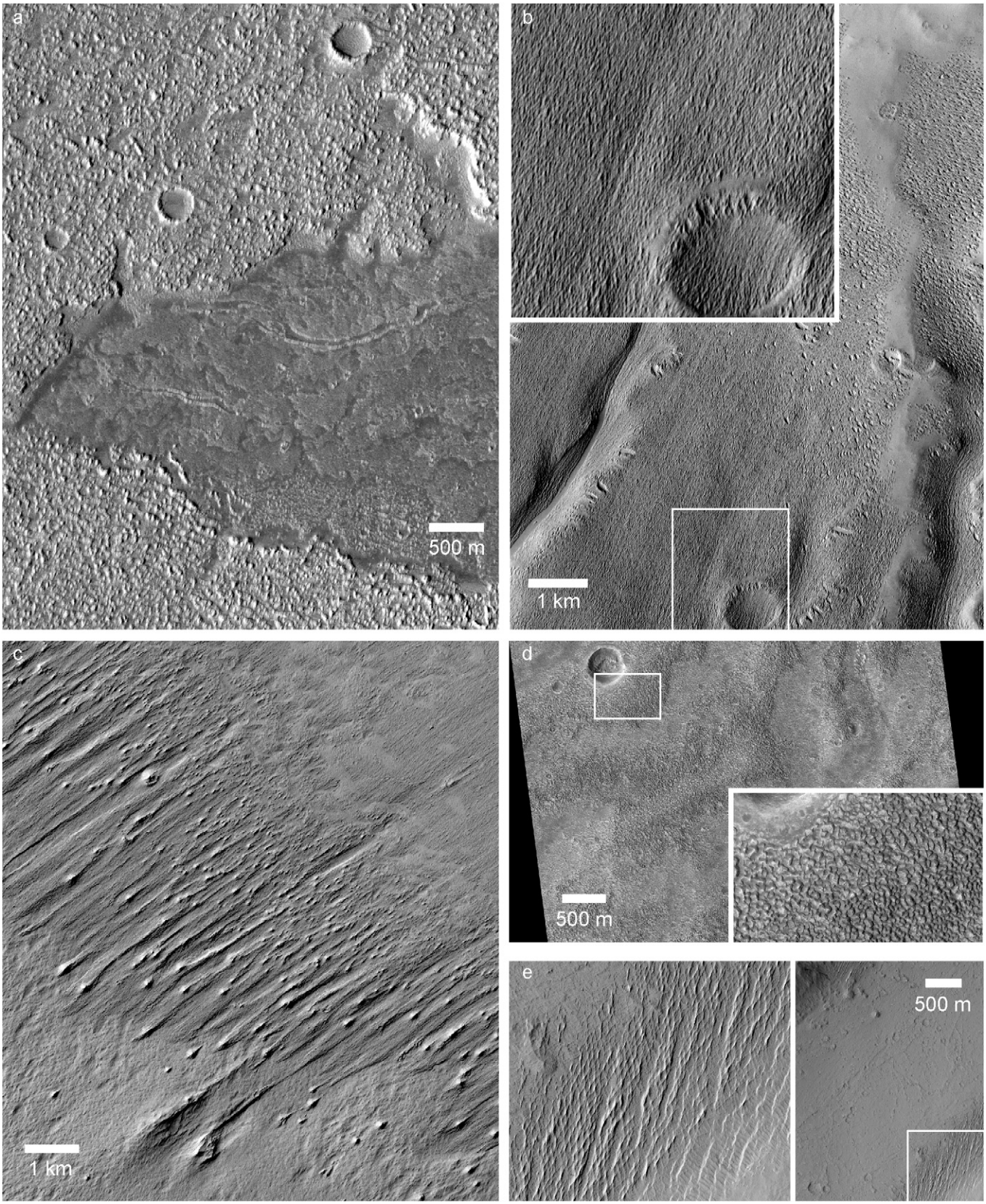

Fig. 4. High resolution images of surfaces designated by white boxes in Figs. 1 and 2. (a) Lava flows south of Arsia Mons (CTX image P08_004188_1622_XN_17S127W; solar inclination 43°). (b) Southwest flank of Apollinaris Patera (CTX image P06_003544_1703_XI_09S185W; solar inclination 52°). (c) Yardangs north of Apollinaris Patera (CTX image P16_007236_1754_XN_04S186W; solar inclination 45°). (d) Valley networks near Warrego Valles (HiRISE image PSP_003699_1380; solar inclination 50°). (e) Lucus Planum (HiRISE image PSP_006576_1815; solar inclination 37°). The highly textured surfaces in each image corresponds with regions that appear various shades of blue in the THEMIS DCS images.

servations that is present in the Apollinaris Patera observations. The TES data show a distinct slope that is consistent with the THEMIS data and the long wavelength spectral character continues the same trend. These results are similar to those of Osterloo et al. (2008) although the TES spectra are more clearly isolated from the surrounding basaltic terrain in the example presented here.

4. Modeled spectra

Synthetic spectra were calculated using the methods described above to evaluate the cause of the spectral slope in the two surface types. It is assumed that the cause of the slope is either anisothermality or low emissivity, but not a combination of the two factors. Each of the two examples described above with repeat TES and THEMIS data coverage were simulated as closely as possible using both the anisothermal and low emissivity models. Only one free parameter is present in each case; θ-bar for the anisothermality model and graybody emissivity in the low emissivity model. The simple nature of the models and parameters is sufficient to isolate the cause of the clearly distinct spectral behavior of the two surface types.

The simulated anisothermal spectra are shown in Figs. 9 and 10. In the case of the simulated Apollinaris Patera observations, increasing values of θ-bar result in more severe spectral slopes in some of the observations and little effect in the simulated TES observation. The result is an increasing disparity in the various measurements with increasing surface slope angles. The simulated unnamed crater spectra have a similar, but less distinct pattern of separation with increasing surface slope angles. In both cases, the simulated TES spectra are not greatly affected by high surface slopes and the long wavelength portion of the spectrum retain a high emissivity.

The simulated graybody spectra are shown in Figs. 11 and 12. At relatively high graybody emissivity values there is a more pronounced slope in simulated THEMIS data than is present in the simulated TES data. Colder surface temperatures result in a more pronounced convex shape between ~800–1200 cm^{-1} as a result of the greater relative influence of the downwelling dust radiance on the apparent emissivity. With decreasing emissivity values, all simulated TES and THEMIS data from both sites exhibit more pronounced spectral slopes, including at longer wavelengths. Also in contrast to the simulated anisothermal spectra, the simulated graybody spectra do not diverge greatly under more extreme conditions (low emissivity).

5. Discussion

The spectral sets shown in the examples from Apollinaris Patera and Terra Serenum show two distinct patterns; (1) the presence or absence of low emissivity at the longer wavelengths measured by TES and; (2) the degree of variability between observations of the same surface. Both of these properties can be used to distinguish between anisothermality and low emissivity as the cause of the spectral slopes. However, the limitations of the datasets used for the analysis may prevent these properties from being clearly distinguished. For example, the limited wavelength range of the THEMIS data preclude the use of longer wavelengths and

Table 1
Observation parameters for the two spectral surface types shown in Figs. 5 and 8.

Observation ID	Local time	L_s	Solar inc.	Surface temp.
Apollinaris Patera (174° E, 9° S)				
I01292010	15.2	350.5	47.6	263.3
I01654003	15.4	5.5	51.6	257.1
I02740006	16.0	46.9	65.7	231.6
I18205002	16.3	359.8	64.8	238.6
TES OCK[a] 5279	13.8	271.5	30.2	295.4
Terra Serenum (181° E, 27° S)				
I07734002	16.8	259.1	63.8	268.3
I15559004	17.3	232.0	72.1	254.9
I16782002	16.3	295.1	57.7	273.0
TES OCK 5304	13.8	272.7	24.8	297

[a] OCK is Orbit Counter Keeper, or the orbit number starting at Mars Global Surveyor (MGS) orbit insertion rather than the start of the nominal MGS mapping mission.

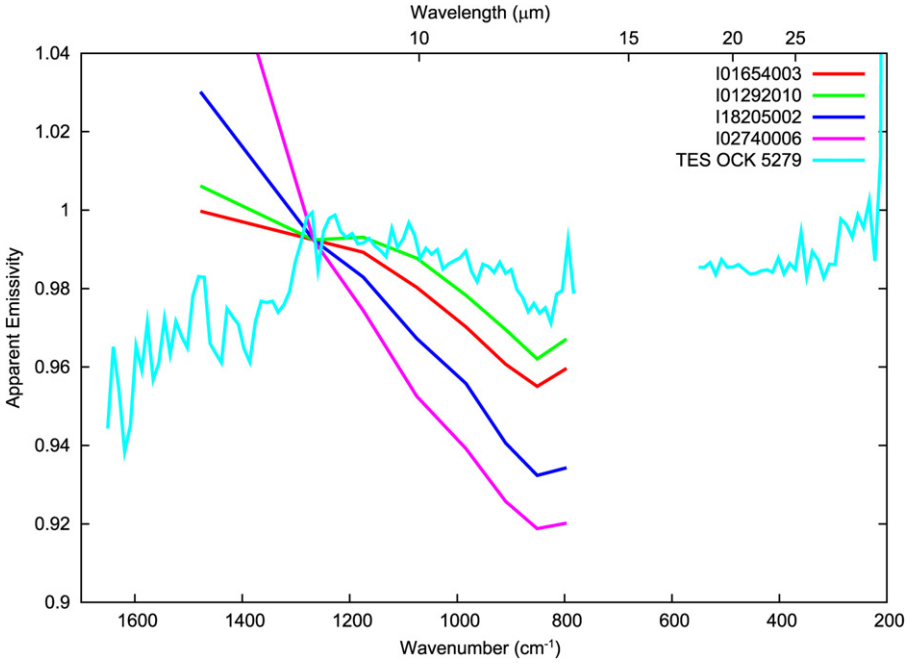

Fig. 5. Surface apparent emissivity spectra from the southwestern flank of Apollinaris Patera derived from several THEMIS and TES observations listed in Table 1 and including data from THEMIS image I02740006 shown in Fig. 1. All spectra, including the lower spatial resolution TES data, cover the same surface.

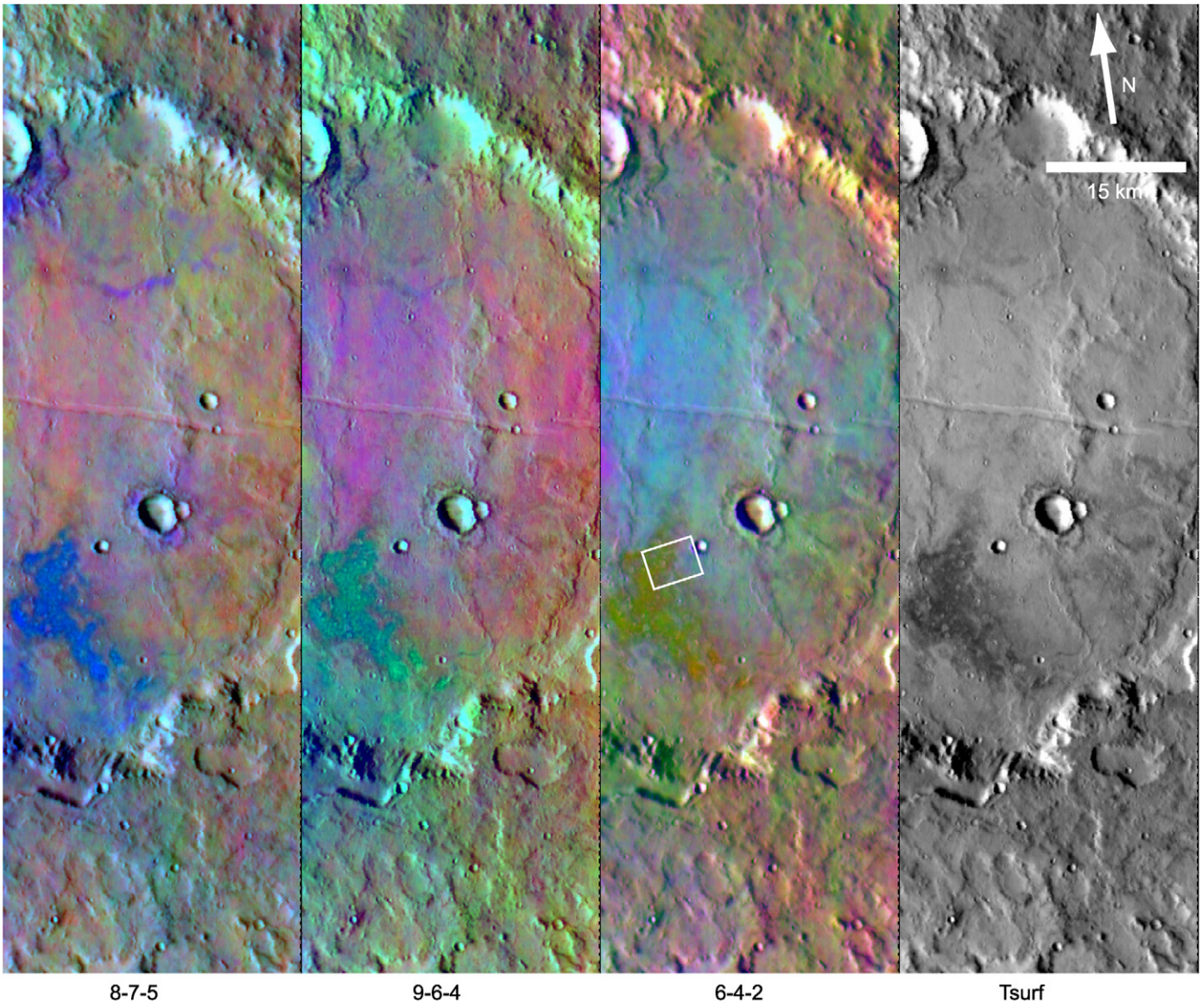

Fig. 6. THEMIS 4-panel image I16782002 centered near 180.65° E, 27° S. The region that is deep blue in the image on the left and relatively cool in the surface temperature image contain the spectral slopes discussed in the text and shown in Fig. 8. The white box indicates the region of the visible image shown in Fig. 7. (For interpretation of the references to color in this figure legend, the reader is referred to the web version of this article.)

the limited local time coverage of the TES data do not allow for the determination of spectral variability from multiple observations.

The Apollinaris Patera spectral set compare well with the simulated anisothermal spectra. The variety of solar inclinations causes varying degrees of anisothermality that result in variable apparent emissivity spectra. In addition, because Planck radiance is a nonlinear function of both temperature and wavelength, the relative change in radiance at different temperatures is dependent on the wavelength of the observation. Under typical martian conditions, this results in a negative spectral slope at wavelengths $< \sim$12 μm, but an overall concave shape that has a positive slope at longer wavelengths (Fig. 13). This concavity is not apparent in the THEMIS data because of the limited wavelength coverage of THEMIS. The nearly complete absence of a spectral slope in the TES data is due to the early afternoon local time conditions of the TES observations that results in a lower degree of anisothermality within the FOV.

Greater surface slopes have larger spectral slope/concavity effects on the spectral sets (Fig. 9) and it is possible to estimate the slope distribution from the data. The spectral sets also display a greater separation between individual observations with increasing surface slopes. Although none of the simulated spectral sets precisely match the Apollinaris Patera TES and THEMIS data, a qualitative comparison indicates that θ-bar values of 20° or 25° (corresponding to RMS slopes of ∼27°–34° using the approximation of Shepard and Campbell, 1998) are in reasonable agreement with the data (Fig. 14). These values are significantly higher than typical for most of the planet derived from multiple emission angle observations (95% of surfaces have θ-bar values <12°; Bandfield and Edwards, 2008). Unfortunately, the large footprint and the coarse gridded sampling of the multiple emission angle observations prevents a direct comparison of the two techniques on these surfaces.

High-resolution imaging displays highly textured surfaces that are directly correlated with the Apollinaris Patera data as well as similar spectral features found at other locations. Based on the solar inclination angles and the common presence of hard shadows, it is likely that the images are resolving the slopes that are influencing the TIR data. Although imaging can be a

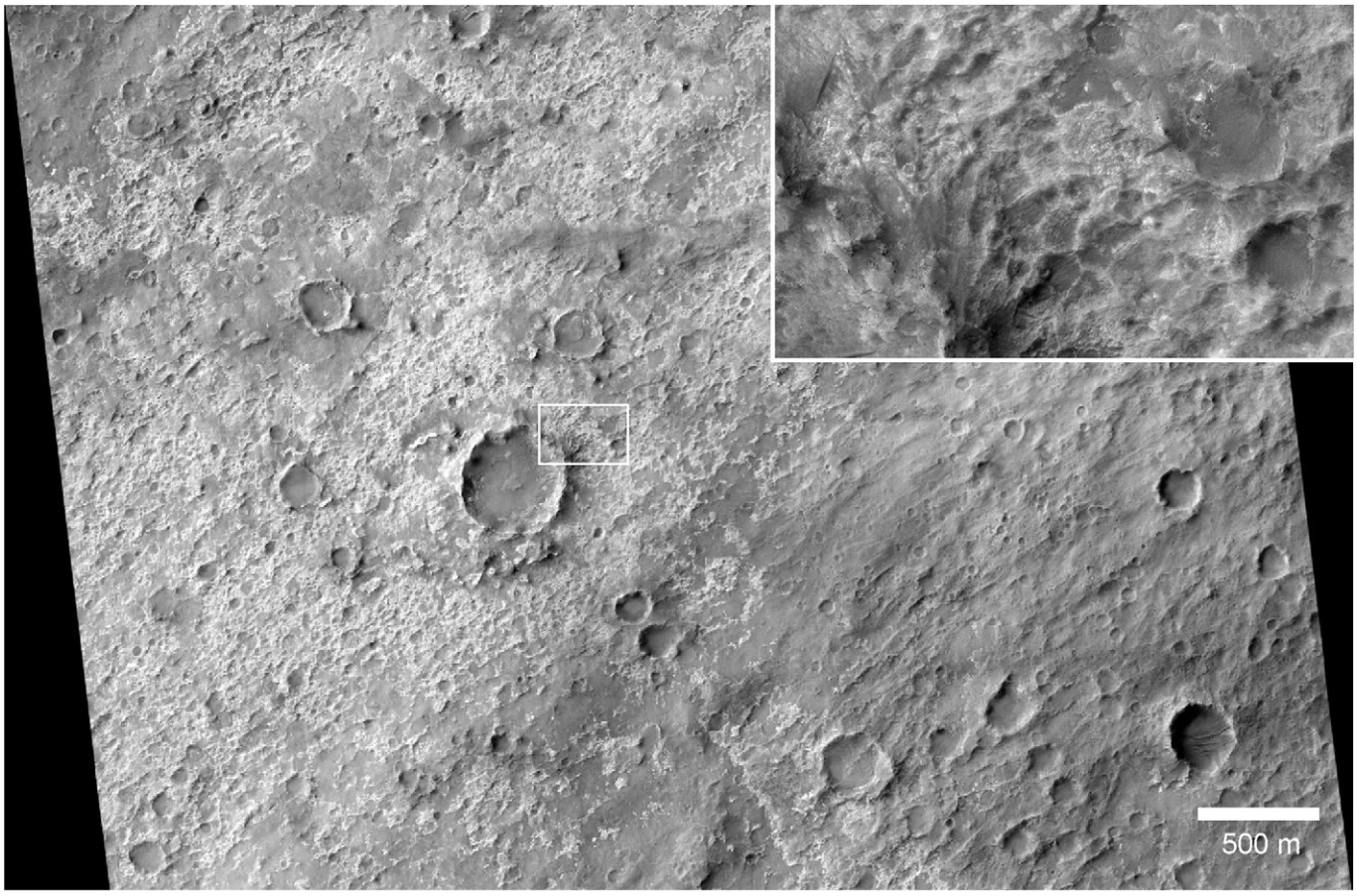

Fig. 7. High resolution image (HiRISE image PSP_005680_1525; solar inclination 35°) of the surface designated by the white box in Fig. 6. Lighter toned surfaces coincide with the spectral slope unit shown in Figs. 6 and 8.

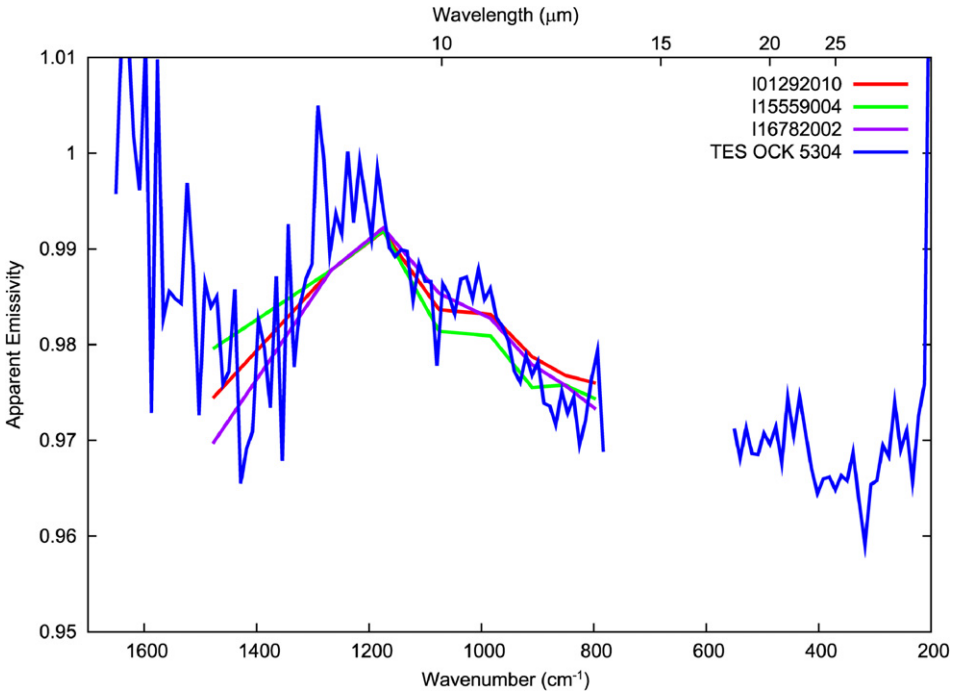

Fig. 8. Surface apparent emissivity spectra from the Terra Serenum region derived from several THEMIS and TES observations listed in Table 1 and including data from THEMIS image I16782002 shown in Fig. 6.

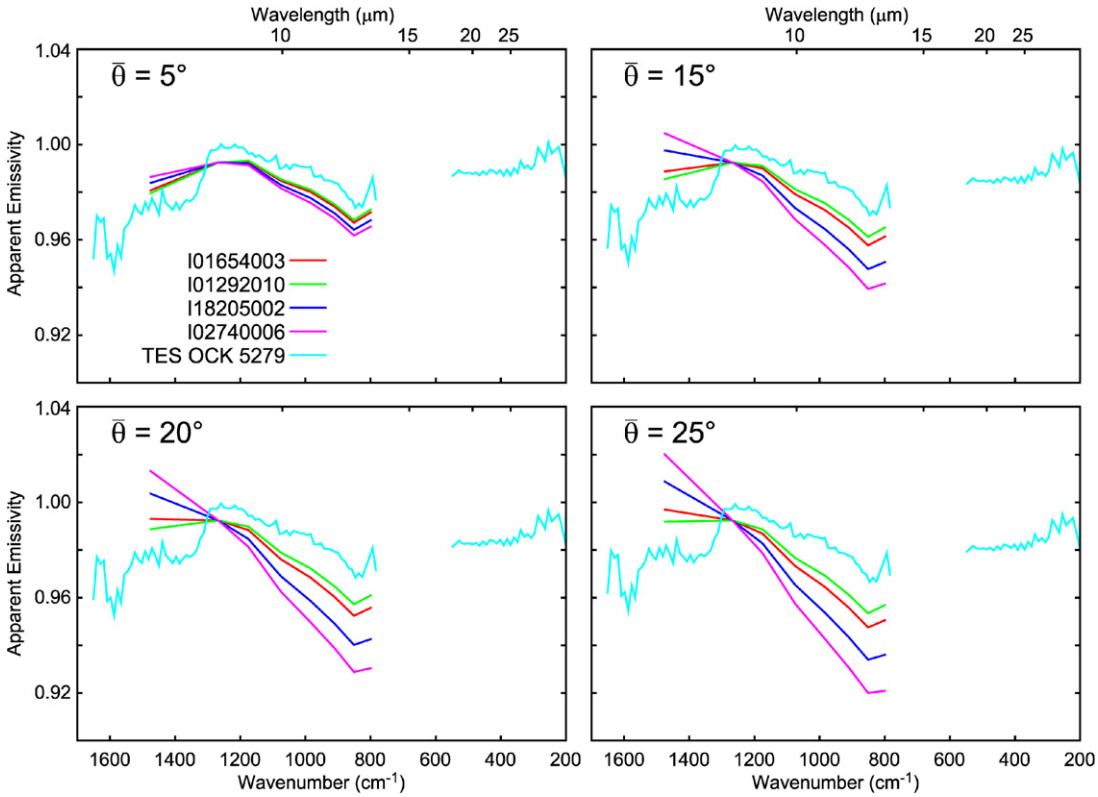

Fig. 9. Simulated apparent emissivity spectra constructed using parameters from the Apollinaris Patera observations listed in Table 1 and plotted in Fig. 5. Spectra for 4 different surface slope distributions using the θ-bar parameter (discussed in the text) are shown. The variations in the spectra are due to the different temperature distributions that result from different local times and seasons for each observation. Steeper slopes result in greater anisothermality and larger differences between each simulated observation. Spectral slopes are not significant in the TES data due to the relatively low solar inclination of the observations that result in a relatively low amount of anisothermality.

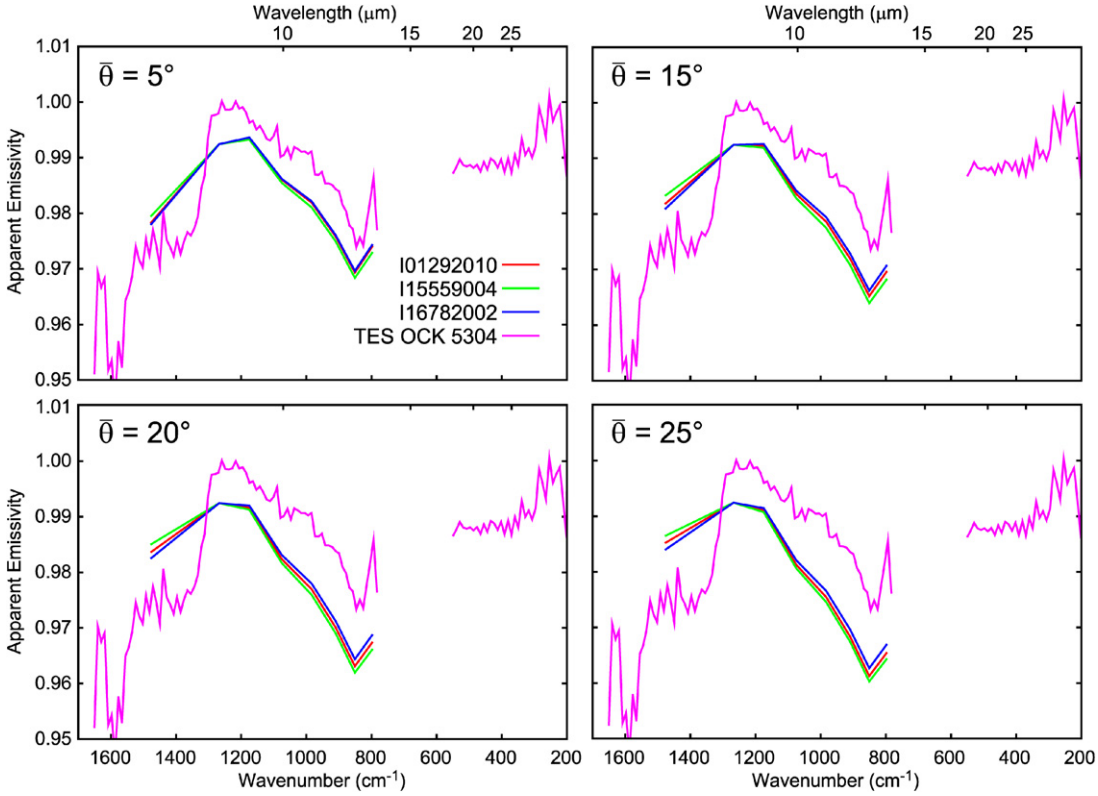

Fig. 10. Simulated apparent emissivity spectra constructed using parameters from the Terra Serenum observations listed in Table 1 and plotted in Fig. 8. Spectra for 4 different surface slope distributions using the θ-bar parameter (discussed in the text) are shown. The conditions present during the collection of the THEMIS data were not highly variable in this case and the contrast between observations is not as large as shown in the Apollinaris Patera case shown in Fig. 9. Significant slopes are not present in the simulated data at long wavelengths, which is inconsistent with the actual measurements.

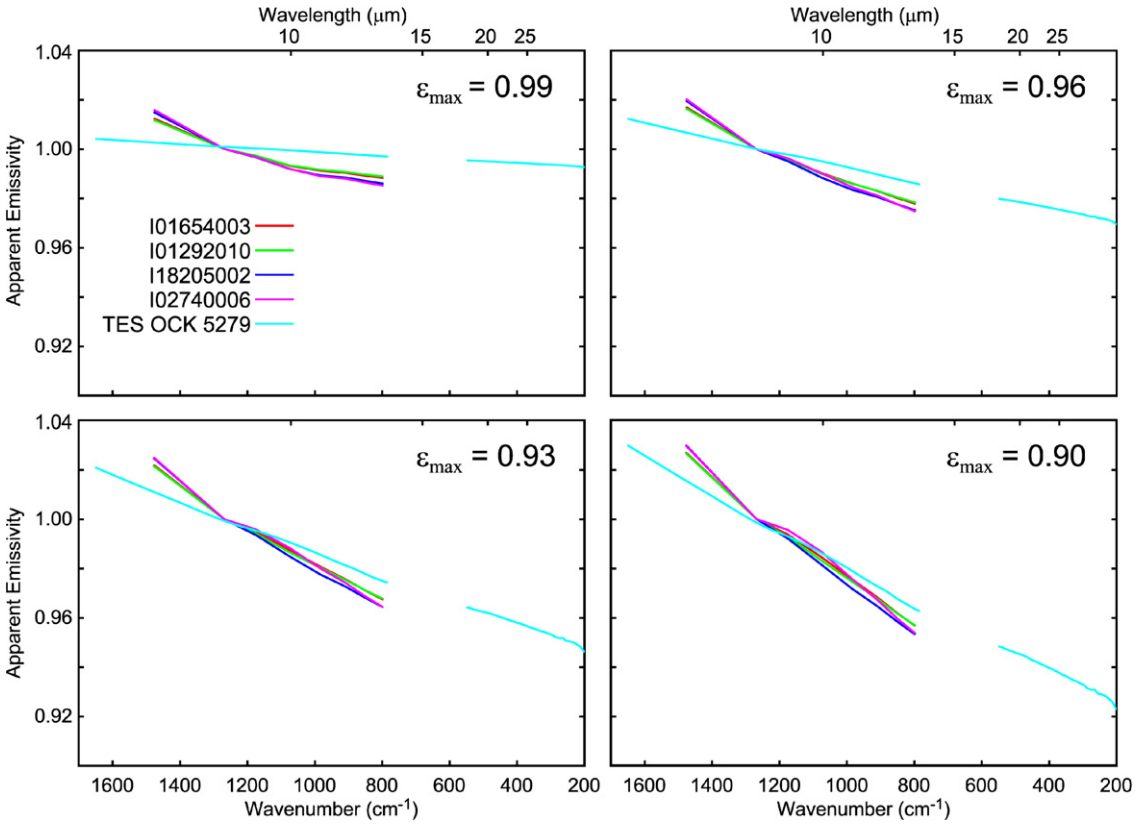

Fig. 11. Simulated apparent emissivity spectra constructed using parameters from the Apollinaris Patera observations listed in Table 1 and plotted in Fig. 5. Spectra for 4 different graybody emissivity values are shown. Changes in the slope of the spectra are relatively uniform compared with the simulated anisothermal spectra shown in Fig. 9. Relatively subtle changes in the shape of the spectra between ~800–1200 cm^{-1} are due to the increasing magnitude of reflected atmospheric radiance with lower overall surface emissivity. Slopes are apparent at long wavelengths in the simulated data that are not present in the actual measurements.

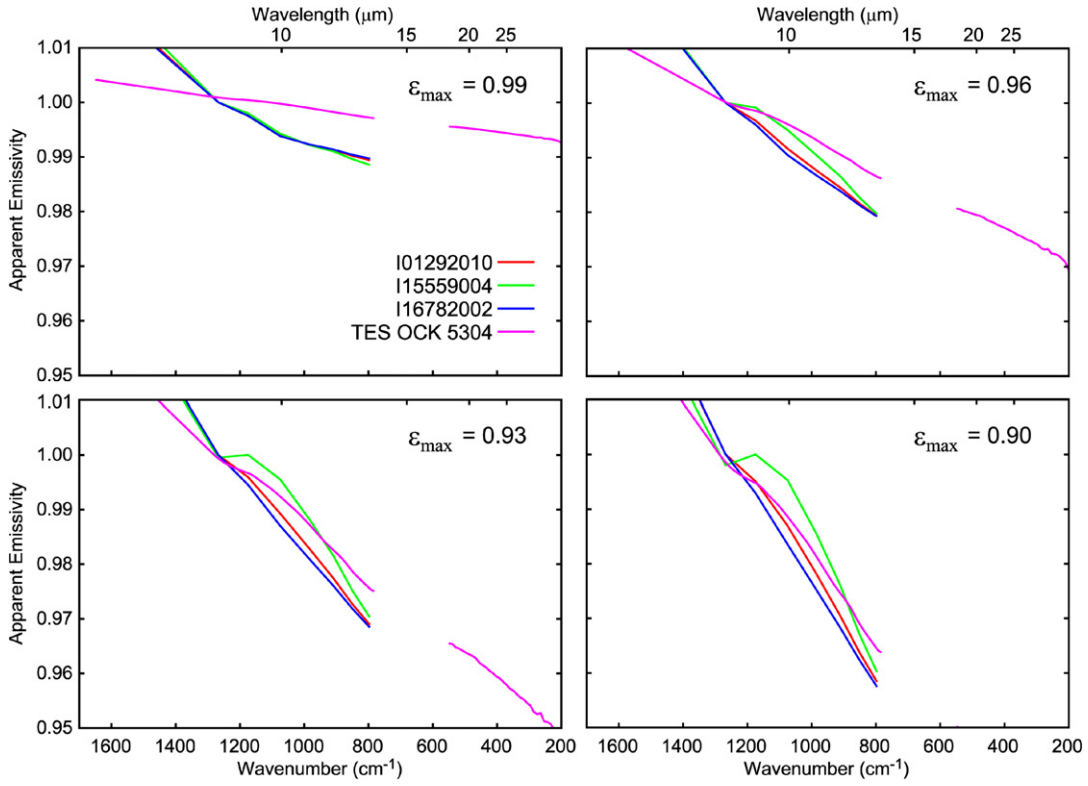

Fig. 12. Simulated apparent emissivity spectra constructed using parameters from the Terra Serenum observations listed in Table 1 and plotted in Fig. 8. Spectra for 4 different graybody emissivity values are shown. The changes in slope with varying emissivity values is greater than that present in the simulated anisothermal data (Fig. 10) and the spectral slopes are predicted to extend to longer wavelengths at the earlier local time of the TES observations.

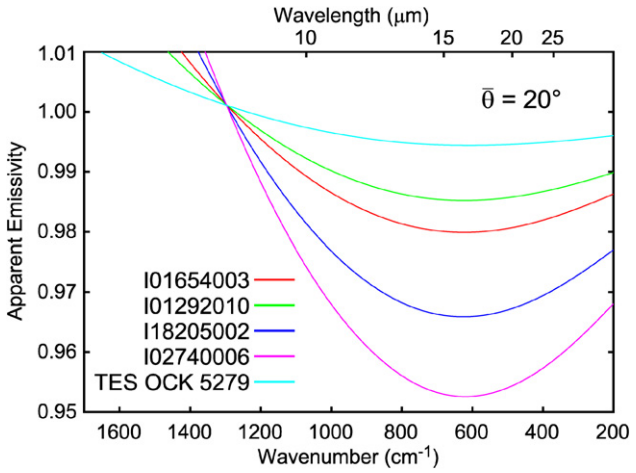

Fig. 13. Simulated apparent emissivity spectra for the θ-bar = 20° case as shown in Fig. 9. In this case all simulated spectra are shown at TES spectral sampling to illustrate the variability in the spectra at longer wavelengths that are not observed with the relatively limited wavelength coverage of THEMIS.

more direct method for identifying surfaces with steep slopes, the THEMIS data provide much greater spatial coverage and are sensitive to scales as small as 1–2 cm in regions of low thermal inertia (Bandfield and Edwards, 2008). The scale of sensitivity is limited to surfaces that can maintain thermal isolation. Much finer scale surface roughness can be derived from the reduction of spectral contrast due to multiple reflections of emitted radiance between adjacent surfaces (e.g. Ramsey and Fink, 1999; Danilina et al., 2006).

It appears that wind-eroded yardangs within the Medusa Fossae formation are the most widespread occurrence of these features (Fig. 3). However, there are also associations with what appears to be dessicated terrain near Warrego Vallis and individual lava flow features south of Arsia Mons. As would be expected, it appears that there are multiple formation mechanisms that lead to the steep surface slopes that result in the characteristic apparent emissivity spectra.

The set of spectra from Terra Serenum are from a narrower range of solar inclination and temperature conditions. As a result, the simulated anisothermal spectra no not display as much diversity as is present in the Apollinaris Patera example. However, the long wavelength character is similar in both simulations and is clearly distinct from that of graybody apparent emissivity effects. The Terra Serenum spectral set display characteristics that are consistent with a low emissivity surface and can be distinguished by the continuation of the negative spectral slope at long wavelengths ($> \sim$15 μm) that is inconsistent with the anisothermal example.

The simulated spectra were calculated using perfect graybodies with no spectral features, whereas the TES and THEMIS spectra from Terra Serenum appear to have some spectral character and there is some suggestion of an emissivity drop off at short wavelengths ($< \sim$8 μm) consistent with a contribution from fine particulate materials in the FOV (Ruff and Christensen, 2002; Bandfield and Smith, 2003). There is no indication that the spectral character is similar to the martian dust as is the case in Apollinaris Patera, particularly because the transparency feature at ~11 μm that is characteristic of the dust is not present. The dusty surface shape also results in an apparent offset in emissivity that is not as apparent in the TES and THEMIS measurements. This offset is due to the relatively wide THEMIS band 3 filter and how it is convolved with the dust spectral shape. Although the simulated graybody spectra are not offset in the same way as the TES and THEMIS data, the consistent overall slope present in both spectral sets provides a reasonable match (Fig. 14).

The locations and morphology from high-resolution images of this spectral surface type has been documented by Osterloo et al. (2008) and described briefly above. There appears to be only a single general morphological type of surface associated with this spectral unit, which does not appear to contain surfaces with high slopes, especially with respect to the surrounding terrain. As described by Osterloo et al. (2008), this surface type is primarily located within Noachian southern highland terrains.

The presence of low emissivity surfaces was attributed by Osterloo et al. (2008) to the presence of chlorides, which typically exhibit low emissivity characteristics that are generally consistent with the TES and THEMIS observations. Regardless of the specific composition responsible for the unique spectral properties, this surface can be attributed to a composition distinct from the surrounding terrain rather than a temperature effect due to physical surface properties.

6. Conclusions

Spectral slopes present in TIR data can generally be attributed to misrepresenting the surface temperature, either through incorrect assumptions about the maximum emissivity of surface materials or the presumption of a uniform surface temperature. These incorrect assumptions leave distinct characteristics in the resulting apparent emissivity data that can be used to gain a better understanding of the surface properties.

Surfaces with high surface slopes typically have a high degree of anisothermality at high angles of solar incidence. The resulting mixture of surface temperatures within the FOV causes distinct slopes in apparent emissivity spectra that can be highly variable based on the observing conditions. These properties are apparent on the southwestern flank of Apollinaris Patera and can be reasonably modeled with a surface slope distribution of θ-bar = 20°–25°. This is an extremely rough surface that exceeds the surface slopes of most surfaces mapped by Bandfield and Edwards (2008). These surfaces coincide with yardangs and other surfaces south of Arsia Mons and near Warrego Valles that appear to have very high slopes in high resolution images.

Surfaces with low maximum values of emissivity have apparent emissivity spectra with more consistent spectral slopes that do not vary greatly based on observing conditions. The spectral surface type of Osterloo et al. (2008) and documented here in Terra Serenum exhibits characteristics consistent with low emissivity surfaces rather than anisothermal surfaces. This is consistent with associated high resolution images that do not indicate the presence of a surface significantly rougher than the surrounding terrain.

Acknowledgments

Thanks to Deanne Rogers, Laura Mayorga, and Jennifer Braun for documenting the distributions of the surface types presented here. Alice Baldridge, Alan Gillespie, Tim Glotch, Vicky Hamilton, Mikki Osterloo, and Steve Ruff provided useful discussions that helped shape the distinction and understanding of the effects of low emissivity and anisothermality presented here. Michael Ramsey and an anonymous reviewer provided constructive and helpful formal reviews that improved the quality of this manuscript. This work was partially supported by NASA Grant NNX08AK52G from the Mars Data Analysis Program.

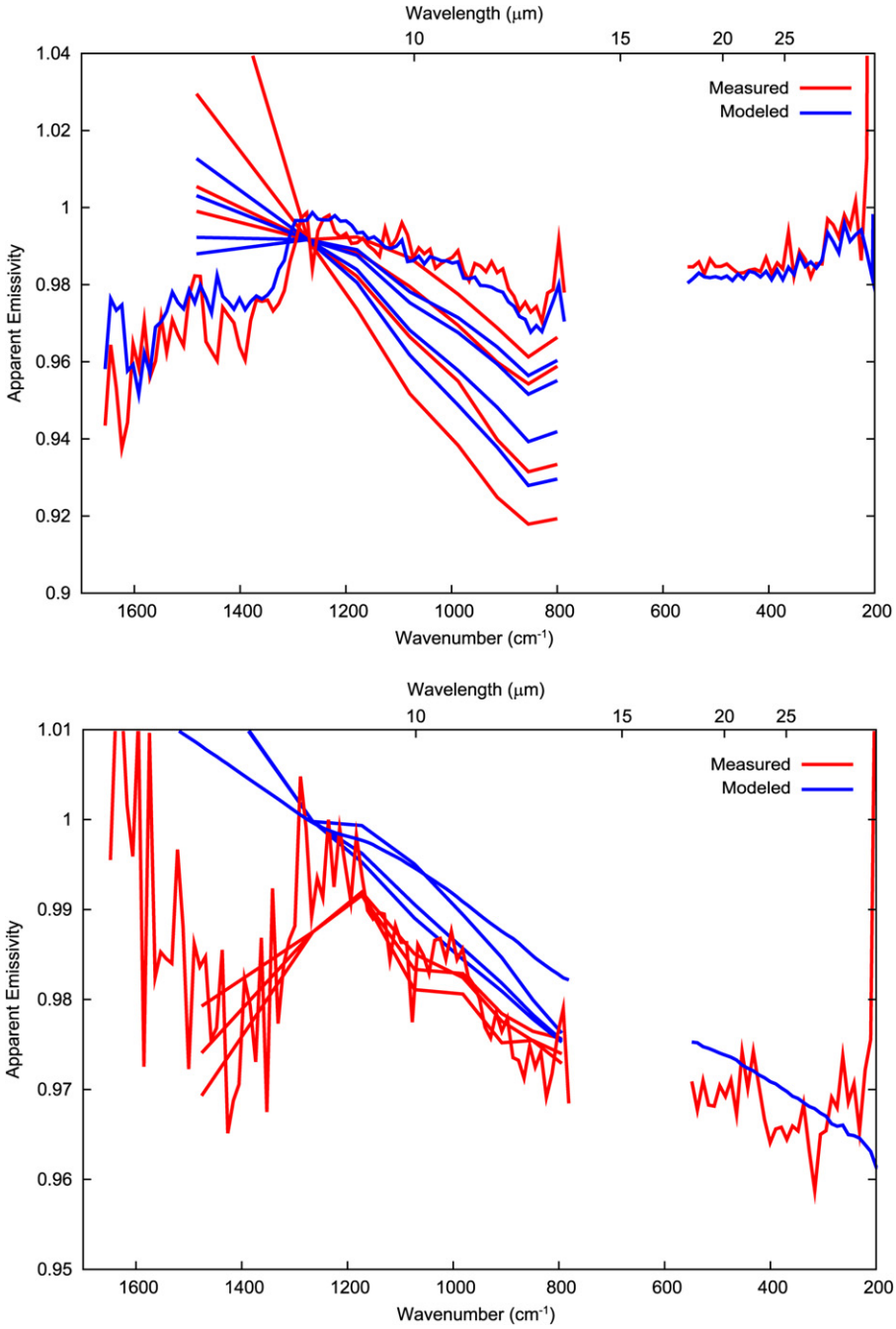

Fig. 14. Direct comparisons of measured (red) and modeled (blue) TES and THEMIS data. The top plot shows data from Apollinaris Patera (Fig. 5) compared with the simulated data with a θ-bar value of 20° (shown in Fig. 9). The bottom plot shows data from Terra Serenum (Fig. 8) compared with the simulated data with a graybody emissivity of 0.95 (shown in Fig. 12). (For interpretation of the references to color in this figure legend, the reader is referred to the web version of this article.)

References

Armstrong, J.C., Titus, T.N., Kieffer, H.H., 2005. Evidence for subsurface water ice in Korolev crater, Mars. Icarus 174, 360–372.

Balick, L.K., Hutchinson, B.A., 1986. Directional thermal infrared exitence distributions from a leafless deciduous forest. IEEE Trans. Geosci. Rem. Sens. GE-24, 693–698.

Bandfield, J.L., 2006. Extended surface exposures of granitoid compositions in Syrtis Major, Mars. Geophys. Res. Lett. 33, doi:10.1029/2005GL025559.

Bandfield, J.L., 2008. High-silica deposits of an aqueous origin in western Hellas Basin, Mars. Geophys. Res. Lett. 35, doi:10.1029/2008GL033807.

Bandfield, J.L., Edwards, C.S., 2008. Derivation of martian surface slope characteristics from directional thermal infrared radiometry. Icarus 193, 139–157.

Bandfield, J.L., Feldman, W.C., 2008. Martian high latitude permafrost depth and surface cover thermal inertia distributions. J. Geophys. Res. 113, doi:10.1029/2007JE003007.

Bandfield, J.L., Smith, M.D., 2003. Multiple emission angle surface–atmosphere separations of thermal emission spectrometer data. Icarus 161, 47–65.

Bandfield, J.L., Rogers, A.D., Smith, M.D., Christensen, P.R., 2004. Atmospheric correction and surface spectral unit mapping using Thermal Emission Imaging System data. J. Geophys. Res. 109, doi:10.1029/2004JE002289.

Christensen, P.R., 1986. The spatial distribution of rocks on Mars. Icarus 68, 217–238.

Christensen, P.R., and 25 colleagues, 2001. Mars Global Surveyor Thermal Emission Spectrometer experiment: Investigation description and surface science results. J. Geophys. Res. 106, 23823–23872.

Christensen, P.R., Jakosky, B.M., Kieffer, H.H., Malin, M.C., McSween Jr., H.Y., Nealson, K., Mehall, G.L., Silverman, S.H., Ferry, S., Caplinger, M., Ravine, M., 2004. The Thermal Emission Imaging System (THEMIS) for the Mars 2001 Odyssey Mission. Space Sci. Rev. 110, 85–130.

Colwell, J.E., Jakosky, B.M., 2002. Effects of topography on thermal infrared spectra of planetary surfaces. J. Geophys. Res. 107, doi:10.1029/2001JE001829.

Conrath, B.J., Pearl, J.C., Smith, M.D., Maguire, W.C., Christensen, P.R., Dason, S., Kaelberer, M.S., 2000. Mars Global Surveyor Thermal Emission Spectrometer (TES)

observations: Atmospheric temperatures during aerobraking and science phasing. J. Geophys. Res. 105, 9509–9520.

Danilina, I., Mushkin, A., Gillespie, A.R., O'Neil, M., Abbott, E.A., Balick, L., 2006. Roughness effects on sub-pixel radiative temperature dispersion ina kinetically isothermal surface. In: Sobrino, J. (Ed.), Proceedings of Second Recent Advances in Quantitative Remote Sensing. Publicacions de la Universitat de Valencia, Valencia, Spain, pp. 13–18.

Fergason, R.L., Christensen, P.R., Kieffer, H.H., 2006a. High-resolution thermal inertia derived from the Thermal Emission Imaging System (THEMIS): Thermal model and applications. J. Geophys. Res. 111. 12004.

Fergason, R.L., Christensen, P.R., Bell III, J.F., Golombek, M.P., Herkenhoff, K.E., Kieffer, H.H., 2006b. Physical properties of the Mars Exploration Rover landing sites as inferred from Mini-TES derived thermal inertia. J. Geophys. Res. 111, doi:10.1029/2005JE002583.

Gillespie, A.R., Kahle, A.B., Walker, R.E., 1986. Color enhancement of highly correlated images. I. Decorrelation and HSI contrast stretches. Rem. Sens. Environ. 20, 209–235.

Gillespie, A., Rokugawa, S., Matsunaga, T., Cothern, J.S., Hook, S., Kahle, A.B., 1998. A temperature and emissivity separation algorithm for Advanced Spaceborne Thermal Emission and Reflection Radiometer (ASTER) images. IEEE Trans. Geosci. Rem. Sens. 36, 1113–1126.

Hapke, B., 1984. Bidirectional reflectance spectroscopy. III. Correction for macroscopic roughness. Icarus 59, 41–59.

Kieffer, H.H., Christensen, P.R., Titus, T.N., 2006. CO_2 jets formed by sublimation beneath translucent slab ice in Mars' seasonal south polar ice cap. Nature 442, doi:10.1038/nature04945.

Li, Z.L., Zhang, R., Sun, X., Su, H., Tang, X., Zhu, Z., Sobrino, J.A., 2004. Experimental system for the study of the directional thermal emission of natural surfaces. Int. J. Rem. Sens. 25, 195–204.

Malin, M.C., Edgett, K.S., 2001. Mars Global Surveyor Mars Orbiter Camera: Interplanetary cruise through primary mission. J. Geophys. Res. 106, 23429–23570.

Malin, M.C., Bell III, J.F., Cantor, B.A., Caplinger, M.A., Calvin, W.M., Clancy, R.T., Edgett, K.S., Edwards, L., Haberle, R.M., James, P.B., Lee, S.W., Ravine, M.A., Thomas, P.C., Wolff, M.J., 2007. Context camera investigation on board the Mars Reconnaissance Orbiter. J. Geophys. Res. 112, doi:10.1029/2006JE002808.

McCabe, M.F., Balick, L.K., Theiler, J., Gillespie, A.R., Mushkin, A., 2008. Linear mixing in thermal infrared temperature retrieval. Int. J. Rem. Sens. 29, 5047–5061.

McEwen, A.S., Eliason, E.M., Bergstrom, J.W., Bridges, N.T., Hansen, C.J., Delamere, W.A., Grant, J.A., Gulick, V.C., Herkenhoff, K.E., Keszthelyi, L., Kirk, R.L., Mellon, M.T., Squyres, S.W., Thomas, N., Weitz, C.M., 2007. Mars Reconnaissance Orbiter's High Resolution Imaging Science Experiment (HiRISE). J. Geophys. Res. 112, doi:10.1029/2005JE002605.

Mushkin, A., Danilina, I., Gillespie, A.R., Balick, L.K., McCabe, M.F., 2007. Roughness effects on thermal-infrared emissivities estimated from remotely sensed images. Proc. SPIE 6749. 6749-2V.

Nowicki, S.A., Christensen, P.R., 2007. Rock abundance on Mars from the Thermal Emission Spectrometer. J. Geophys. Res. 112, doi:10.1029/2006JE002798.

Osterloo, M.M., Hamilton, V.E., Bandfield, J.L., Glotch, T.D., Baldridge, A.M., Christensen, P.R., Tornabene, L.L., Anderson, F.S., 2008. Chloride-bearing materials in the Southern highlands of Mars. Science 319, doi:10.1126/science1150690.

Ramsey, M.S., Fink, J.H., 1999. Estimating silicic lava vesicularity with thermal remote sensing: A new technique for volcanic mapping and monitoring. Bull. Volcanol. 61, 32–39. Abstract 8c_12.

Ramsey, M.S., Kuhn, S., 2004. Fusion of parametric and thematic data to characterize the Soufrière Hills Volcanic Dome. In: Abstr. of the Gen. Assembly IAVCEI. Abstract 8c_12.

Ruff, S.W., Christensen, P.R., 2002. Bright and dark regions on Mars: Particle size and mineralogical characteristics based on Thermal Emission Spectrometer data. J. Geophys. Res. 107, doi:10.1029/2001JE001580.

Ruff, S.W., Christensen, P.R., Barbera, P.W., Anderson, D.L., 1997. Quantitative thermal emission spectroscopy of minerals: A laboratory technique for measurement and calibration. J. Geophys. Res. 102, 14899–14913.

Ruff, S.W., Christensen, P.R., Blaney, D.L., Farrand, W.H., Johnson, J.R., Michalski, J.R., Moersch, J.E., Wright, S.P., Squyres, S.W., 2006. The rocks of Gusev Crater as viewed by the Mini-TES instrument. J. Geophys. Res. 111, doi:10.1029/2006JE002747.

Shepard, M.K., Campbell, B.A., 1998. Shadows on a planetary surface and implications for photometric roughness. Icarus 134, 279–291.

Smith, J.A., Chauhan, N.S., Schmugge, T.J., Ballard Jr, J.R., 1997. Remote sensing of land surface temperature: The directional viewing effect. IEEE Trans. Geosci. Rem. Sens. 35, 972–974.

Smith, M.D., 2004. Interannual variability in TES atmospheric observations of Mars during 1999-2003. Icarus 167, 148–165.

Smith, M.D., Bandfield, J.L., Christensen, P.R., 2000a. Separation of surface and atmospheric spectral features in Mars Global Surveyor Thermal Emission Spectrometer (TES) spectra. J. Geophys. Res. 105, 9589–9608.

Smith, M.D., Pearl, J.C., Conrath, B.J., Christensen, P.R., 2000b. Mars Global Surveyor Thermal Emission Spectrometer (TES) observations of dust opacity during aerobraking and science phasing. J. Geophys. Res. 105, 9539–9552.

Titus, T.N., Kieffer, H.H., Christensen, P.R., 2003. Exposed water ice discovered near the South Pole of Mars. Science 299, 1048–1051.

Zhang, R.H., Li, Z.L., Tang, X.Z., Sun, X.M., Su, H.B., Zhu, C., Zhu, Z.L., 2004. Study of emissivity scaling and relativity of homogeneity of surface temperature. Int. J. Rem. Sens. 25, 245–259.